Phase-selective sol–gel auto-combustion synthesis of γ-Fe_2O_3 and Fe_3O_4 nanoparticles

J.P. Miranda Murillo, M. Abdolrahimi, N. Yaacoub, F. Talaee Shoar, G. Barucca, G. Varvaro, A. Ghary Haghighat, A. Ramzan, E. Segueni, S. Ammar, S. Slimani, P. Manfrinetti, P. Maltoni, A. Omelyanchik,* and D. Peddis*

Received: 12 September 2025 / Accepted: 24 November 2025 / Published online: 16 March 2026

This study presents a roadmap for the controlled sol–gel auto-combustion synthesis of magnetite (Fe_3O_4) and maghemite (γ-Fe_2O_3) nanoparticles, with a focus on the influence of atmospheric conditions during the synthesis process. Combustion in ambient air results in a mixture of hematite (α-Fe_2O_3) and spinel-type iron oxides (Fe_3O_4/γ-Fe_2O_3), as confirmed by x-ray diffraction and magnetic measurements. In contrast, combustion performed in a tubular oven under air predominantly yields the γ-Fe_2O_3 phase. When the process is conducted under an argon atmosphere, nearly pure Fe_3O_4 nanoparticles are obtained, exhibiting high saturation magnetization (~74 Am^2kg^{-1} at 300 K) and a clear Verwey transition at ~117 K. Additionally, Mössbauer spectrometry study confirmed formation of distinct iron oxide phases by different hyperfine parameters. The scalability and reproducibility of the argon-based synthesis were demonstrated across 20 independent batches, all displaying consistent structural and magnetic characteristics. Post-synthesis annealing in air further elucidates the thermal phase transformation from Fe_3O_4/γ-Fe_2O_3 to α-Fe_2O_3 at elevated temperatures. These findings underscore the pivotal role of atmospheric control in tailoring the phase composition and magnetic properties of iron oxide nanoparticles.

Introduction

Iron oxides, such as magnetite (Fe_3O_4), maghemite (γ-Fe_2O_3), and hematite (α-Fe_2O_3), have attracted significant attention in the field of materials science due to physico–chemical and magnetic properties, highly valuable for various applications such as medicine, environmental remediation, and catalysis.[1–6] Two polymorphs with the spinel structure, Fe_3O_4 and γ-Fe_2O_3, are

Impact statement

This work advances the synthesis of iron oxide nanoparticles by introducing a simple and scalable sol–gel auto-combustion (SGAC) that can selectively yield either magnetite (Fe_3O_4) or maghemite (γ-Fe_2O_3). Spinel iron oxides are central to multiple fields, ranging from geoscience and archaeology to biomedical imaging, catalysis, and data storage. However, controlling which phase is obtained remains a long-standing challenge because of their structural similarity and overlapping magnetic responses. Our study demonstrates that controlling the synthesis atmosphere in SGAC governs phase formation, enabling the reproducible preparation of high-purity magnetite or maghemite.

Importantly, magnetite samples exhibit a clear Verwey transition — a key electronic ordering phenomenon — providing a reliable fingerprint of phase purity and stoichiometry. The ability to systematically compare the two phases synthesized under identical conditions provides new insights into oxidation-driven transformations in spinel iron oxides.

Beyond the fundamental interest, this work offers a practical pathway toward producing well-defined iron oxide nanomaterials at scale, without relying on expensive precursors or complex processing. By bridging fundamental mechanisms with reproducible synthesis strategies, our results are relevant not only to materials chemists but also to researchers developing technologies in energy, environment, medicine, and information storage.

J.P. Miranda Murillo, Department of Chemistry and Industrial Chemistry & INSTM RU, nM2-Lab, Università di Genova, 16146 Genoa, Italy
M. Abdolrahimi, Department of Chemistry and Industrial Chemistry & INSTM RU, nM2-Lab, Università di Genova, 16146 Genoa, Italy; Institute of Structure of Matter, National Research Council, nM2-Lab, 00015 Rome, Italy
N. Yaacoub, Institut des Molécules et Matériaux du Mans, CNRS UMR-6283, Le Mans Université, 72085 Le Mans, France
F. Talaee Shoar, Department of Chemistry and Industrial Chemistry & INSTM RU, nM2-Lab, Università di Genova, 16146 Genoa, Italy; Dipartimento SIMAU, Università Politecnica delle Marche, 60131 Ancona, Italy
G. Barucca, Dipartimento SIMAU, Università Politecnica delle Marche, 60131 Ancona, Italy
G. Varvaro, Institute of Structure of Matter, National Research Council, nM2-Lab, 00015 Rome, Italy
A. Ghary Haghighat, Department of Chemistry and Industrial Chemistry & INSTM RU, nM2-Lab, Università di Genova, 16146 Genoa, Italy; Dipartimento di Scienze, Università degli Studi Roma Tre, 00146 Rome, Italy
A. Ramzan, Department of Chemistry and Industrial Chemistry & INSTM RU, nM2-Lab, Università di Genova, 16146 Genoa, Italy
E. Segueni, Department of Chemistry and Industrial Chemistry & INSTM RU, nM2-Lab, Università di Genova, 16146 Genoa, Italy; Université Paris Cite, CNRS, ITODYS (UMR-7086), 75205 Paris, France
S. Ammar, Université Paris Cite, CNRS, ITODYS (UMR-7086), 75205 Paris, France
S. Slimani, Department of Chemistry and Industrial Chemistry & INSTM RU, nM2-Lab, Università di Genova, 16146 Genoa, Italy; Institute of Structure of Matter, National Research Council, nM2-Lab, 00015 Rome, Italy
P. Manfrinetti, Department of Chemistry and Industrial Chemistry & INSTM RU, nM2-Lab, Università di Genova, 16146 Genoa, Italy
P. Maltoni, Department of Chemistry and Industrial Chemistry & INSTM RU, nM2-Lab, Università di Genova, 16146 Genoa, Italy; Institute of Structure of Matter, National Research Council, nM2-Lab, 00015 Rome, Italy
A. Omelyanchik, Department of Chemistry and Industrial Chemistry & INSTM RU, nM2-Lab, Università di Genova, 16146 Genoa, Italy; Institute of Structure of Matter, National Research Council, nM2-Lab, 00015 Rome, Italy; aleksander.omelianchik@ext.unige.it
D. Peddis, Department of Chemistry and Industrial Chemistry & INSTM RU, nM2-Lab, Università di Genova, 16146 Genoa, Italy; Institute of Structure of Matter, National Research Council, nM2-Lab, 00015 Rome, Italy; davide.peddis@unige.it
*Corresponding author

doi:10.1557/s43577-025-01045-z

ferrimagnetic materials with a saturation magnetization (M_S) at 300 K of ~91 and ~73 Am^2kg^{-1}, respectively.[7,8] Although Fe_3O_4 features a slightly higher magnetic response, γ-Fe_2O_3 has a higher chemical stability, electrical resistivity, and biocompatibility.[9–12] Hematite, instead, exhibits antiferromagnetic properties at cryogenic temperatures and weak ferrimagnetic properties above the first-order spin-flop Morin transition (~260 K), where it possesses an uncompensated moment of ~0.5 Am^2kg^{-1} due to spin canting between the two magnetic sublattices.[13–15] Beyond its magnetic behavior, hematite's high chemical stability and semiconducting nature make it attractive for applications in catalysis,[16–18] pigments,[19,20] and gas sensors.[21]

The crystal structures of all these oxides play a crucial role in their magnetic order and the resulting physical and chemical characteristics. Fe_3O_4 is a mixed-valence iron oxide with Fe^{II} located in octahedral (O_h) and Fe^{III} equally distributed in both octahedral (O_h) and tetrahedral (T_d) sites. Consequently, Fe_3O_4 at room temperature is an inverse spinel oxide belonging to the space group $Fd\bar{3}m$.[4,7,13] The structure of γ-Fe_2O_3 can be considered as a defective magnetite structure composed exclusively of Fe^{III} cations compensated by cation vacancies to maintain charge neutrality.[12] These vacancies could be distributed randomly, forming cubic order or long-range tetragonal superstructures on O_h-coordinated sites.[22] On the other hand, α-Fe_2O_3 crystallizes in the rhombohedral corundum-type structure with space group $R\bar{3}c$.[5]

The interconversion among the various iron oxide phases previously discussed is a synthetic process that can be controlled by heating in specific atmospheric conditions. In particular, the transformation from magnetite to maghemite and subsequently to hematite, occurs progressively with increasing temperature in the presence of oxygen:[23–27]

$$4Fe_3O_4 + O_2 \xrightarrow{<300^\circ C} 6\gamma\text{-}Fe_2O_3 \xrightarrow{\gtrsim(300-400)^\circ C} 6\,\alpha\text{-}Fe_2O_3. \quad (1)$$

The temperature intervals in this transformation pathway can be considered approximate, as the formation of intermediates strongly depends on the effective surface of the sample. At the nanoscale, this oxidation sequence is particularly sensitive to both the oxygen partial pressure and the particle size of the precursor oxide.[4,12,24,27,28] It was shown that Fe_3O_4 nanoparticles start being oxidized to γ-Fe_2O_3 when heated at already 100°C in air, forming a partially ordered vacancy structure with space group $P4_132$ or $P4_332$. Upon further heating to 300–400°C, a fully ordered γ-Fe_2O_3 with space group $P4_12_12$ or $P4_32_12$ can be obtained.[29] Thus, although iron oxide nanoparticles can be synthesized by a variety of chemical routes, the detailed mechanisms underlying their phase transformations and structural ordering remain under active investigation.[22,24,30–35]

Over the past three decades, numerous advanced synthesis strategies have been developed to fabricate nanostructured iron oxides with fine control over their structural, morphological, and chemical characteristics. Among these, micellar routes,[36] thermal decomposition of Fe–citrate complexes,[37] surfactant-assisted high-temperature decomposition techniques,[38] the polyol method,[39] and their tailored combinations have been extensively explored for the rational design of novel magnetic nanostructured materials.[40,41] A major limitation of these methodologies lies in the relatively low yields achievable at the laboratory scale (typically 100–300 mg), which significantly constrains their applicability in large-scale technological domains. In this framework, the sol–gel auto-combustion (SGAC) method has become a promising synthetic strategy for preparing a large variety of metal–oxide nanoparticles due to its short preparation time, low energy consumption, and environmental friendliness.[42,43] In addition, this method shows a relatively high yield (gram order) on the laboratory scale.

As already discussed in the literature,[42,44,45] the SGAC proceeds through sequential stages involving gel formation, dehydration, ignition, and redox decomposition of Fe–citrate complexes. Summarizing:

1. formation of Fe–citrate complexes in solution;
2. gelation through dehydration and cross-linking;
3. thermal decomposition of metal–organic species with the release of gases;
4. redox reaction between nitrates (oxidizers) and the organic fuel (citric acid), forming Fe_3O_4 as the primary oxide.

Subsequent oxidation of Fe_3O_4 under oxygen-rich conditions leads to the formation of γ-Fe_2O_3 and could further promote transformation to α-Fe_2O_3. In the combustion step (step 4), upon heating, rapid dehydration and ignition promote gel swelling and the evolution of gases such as CO_2, H_2O, and N_2, which provide internal porosity and initiate the self-sustained combustion.[42,43] The literature reports several studies for synthesizing Fe_3O_4, γ-Fe_2O_3, and α-Fe_2O_3 by SGAC methods under different conditions.[44–53] In particular, Deshpande et al. studied the effects of oxidizer-fuel selection on SGAC synthesis of Fe_3O_4 or α-/γ-Fe_2O_3 mixtures by heating an iron(III)-citrate gel in argon or air atmospheres.[44,54] The authors suggest a two-step mechanism in which the formed Fe_3O_4 powder leads to the α-/γ-Fe_2O_3 polymorph formation when the as-burnt powder is exposed to environmental oxygen. This approach allows control over the presence of the α-phase, with a simple setup, using economical resources such as iron nitrate, citric acid, and water. Later, other authors reported similar approaches using different fuels or strategies to avoid using the inert atmosphere.[55–57]

The resulting powders from the SGAC process are usually a mixture of mostly both α- and γ-Fe_2O_3 phases.[52] According to R. Ianoş et al.,[57] the combustion of the xerogel composed of Fe–citrate complexes in the air promotes the rapid oxidation of Fe^{2+} to Fe^{3+} due to oxygen in the air, resulting in a mixture of α-Fe_2O_3 and γ-Fe_2O_3. However, the combustion in the absence of air leads to the formation of Fe_3O_4, independently of the ligand used as a precursor of

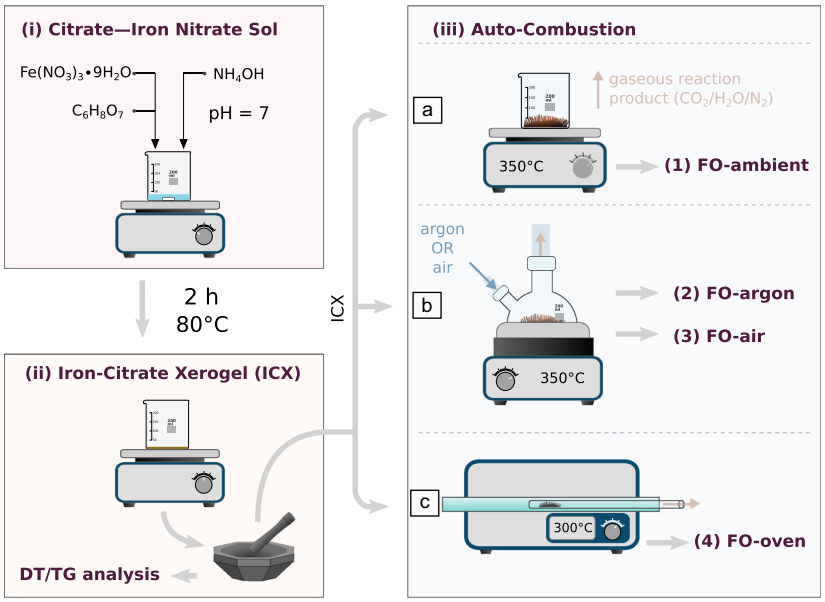

Figure 1. Schematic illustration of the synthesis route for iron oxide nanoparticles using the sol–gel auto-combustion (SGAC) method: preparation of (i) citrate–iron nitrate sol and (ii) iron(III)-citrate xerogel (ICX); (iii) auto-combustion reaction of ICX was carried out under different conditions: (a) on a hot plate in ambient air (FO-ambient), (b) in a two-neck flask under argon (FO-argon) or airflow (FO-air), and (c) in a tubular oven (FO-oven). ICX was also subjected to differential thermal/thermogravimetric (DT/TG) analysis.

the gel (e.g., citric acid, sucrose, or glucose). Cannas et al.[45] reported that γ-Fe_2O_3 nanoparticles could be obtained by a SGAC process in a preheated oven at temperatures from 290°C up to 325°C, while above these temperatures, α-Fe_2O_3 is also formed.

Despite the extensive research, achieving single-phase nanoparticles and understanding the conditions controlling the synthesis of specific desired Fe_3O_4/γ-Fe_2O_3 phase remains challenging. This void seems to be due also to the intrinsic complexity in distinguishing Fe_3O_4 from γ-Fe_2O_3 by using x-ray diffraction (XRD).[58] In addition, they exhibit quite similar magnetic properties at the nanoscale, such as M_S and coercivity (H_C).[31,59] However, a first-order phase transition at ~117 K, referred to as the Verwey transition (T_V), is a fingerprint of Fe_3O_4 that can be observed in the temperature dependence of magnetization or transport properties.[31,60] The Verwey transition is attributed to the ordering of ferrous and ferric ions in the interstitial sites with octahedral and tetrahedral symmetry.[61] For temperatures above T_V, the distribution can be expressed as (Fe^{3+})[$Fe^{2.5+}$], indicating a mixed-valence state. However, below T_V it changes to (Fe^{3+})[Fe^{3+},Fe^{2+}], indicating charge ordering. This charge ordering is accompanied by a structural change, where Fe^{3+} and Fe^{2+} ions in the Oh interstitial sites arrange themselves alternately along the (001) planes, causing a transition from cubic to an orthorhombic crystal structure.

In this work, we demonstrate the phase-selective SGAC synthesis of both Fe_3O_4 and γ-Fe_2O_3 nanoparticles. While earlier works only investigated the preparation of maghemite,[45,62] here we extend this approach to include magnetite obtained under controlled conditions. To the best of our knowledge, this is the first report to explicitly address the Verwey transition in SGAC-derived magnetite nanoparticles, linking synthesis conditions to phase purity and low-temperature electronic ordering. The synthesis was carried out under different atmospheres, including ambient air and argon atmosphere (either in the reactor vessels equipped with a heat source or in a tubular oven). Postannealing studies in air were also conducted to give new insights into the transformation among different iron oxides. In addition, the reproducibility of the SGAC method was investigated, providing new insights about the potential scalability of the process. In summary, our results not only highlight the critical role of atmosphere control in obtaining spinel iron oxide nanoparticles with a preferential phase, but also offer a comprehensive overview of the SGAC method.

Experimental section

Synthesis of iron oxide nanoparticles

Iron oxide nanoparticles were prepared with the SGAC method using citrate–iron nitrate precursors with some modifications.[45] Ferric nitrate nonahydrate $Fe(NO_3)_3 \cdot 9H_2O$ (Aldrich, 98%) and citric acid $C_6H_8O_7$ (CA, Aldrich, 99.9%) were mixed with a magnetic stirrer (300 rpm) in de-ionized water to obtain a solution with a 1:1 molar Fe^{III}/CA ratio in a beaker. Ammonium hydroxide NH_4OH (Aldrich, NH_3 30%) was then added dropwise under constant stirring to adjust the pH up to 7. The clear solution was heated on a hot plate, at ~80°C for 2 h, until the three-dimensional cross-linked network iron(III)-citrate xerogel (ICX) formed after solvent evaporation. The temperature was monitored using the built-in hot plate sensor. The resulting ICX was ground in an agate mortar before the following annealing steps.

The subsequent ICX combustion was performed via several routes (**Figure** 1).

Open-air combustion ("FO-ambient")

The annealing of ICX was carried out directly in the reaction vessel on a preheated hot plate in air at 350°C for ~3 min. Because heating was performed in a tall vessel, no material loss occurred during combustion. The as-obtained powder

exhibited different colors, indicating inhomogeneity in phase composition. This has already been observed and discussed in previous papers.[45,62]

The obtained powders were divided into several batches of equal amounts to conduct a systematic study of the magnetic properties. Each batch was subjected to postannealing in an oven under an air atmosphere for 1 h at 500, 600, 700, and 800°C, respectively. We refer to them as "FO-*xxx*," where "*xxx*" denotes the temperature of thermal treatment.

Controlled inert atmosphere combustion ("FO-argon")

For the FO-argon sample, the ICX was transferred into a two-neck flask connected to a Schlenk line. The atmosphere was purged by three evacuation/argon refill cycles to remove residual air. Subsequently, combustion was performed at 350°C under a continuous flow of high-purity argon for ~3 min.

Combustion in airflow ("FO-air")

This sample was prepared as the "FO-argon" sample but in airflow instead of argon, for comparison.

Combustion in a tubular oven ("FO-oven")

The ICX was placed in a quartz tube (~1 cm in diameter) and inserted into the central zone of a tubular furnace. Combustion was carried out at 350°C for 10 min. After cooling to room temperature under air, the powders were collected.

All resulting powders were subsequently ground again with an agate mortar and pestle to ensure homogeneity and were investigated without any further purification.

Morpho-structural and magnetic characterization

Thermogravimetric (TG) and differential thermal (DT) analyses of citric acid (powder) and ICX were carried out on a Mettler Toledo TGA/SDTA 851 in the range of 100–400°C with a heating rate of 10°C·min^{-1} under oxygen and argon flows (flow rate = 50 ml·min^{-1}). For all analyses, ~10 mg of material was placed in an alumina crucible.

The XRD patterns were acquired with a MiniFlex (Rigaku) diffractometer using a Cu Kα anode (λ = 1.54184 Å) in the 2θ geometry in the range of 30–80°. Data were collected with a step size of 0.01° and a counting time of 1 s per step. The size of crystallites (D_{XRD}) of all the samples was calculated using the Scherrer formula:[63]

$$D_{XRD} = 0.94\lambda/B\cos\theta. \quad (2)$$

B is the full width at half maximum (FWHM) estimated after fitting the XRD peaks with the pseudo-Voigt function, and θ is the Bragg angle corresponding to the peak position. The lattice parameter a for the cubic spinel structure was calculated using the following equation:

$$a = d_{hkl}\sqrt{h^2 + k^2 + l^2}, \quad (3)$$

where d_{hkl} is the interplanar spacing, and h, k, and l are the corresponding Miller indices. The interplanar spacing, d_{hkl}, was obtained using Bragg's Law.

Transmission electron microscopy (TEM) observations were performed using a Philips CM200 microscope operating at 200 kV and equipped with a LaB_6 electron source.

Field-dependent magnetization loops were measured at 300 K by using a vibrating sample magnetometer (VSM Model 10–Microsense) equipped with an electromagnet producing magnetic fields in the range from −2 T to +2 T. The saturation magnetization, M_S, was calculated using the law of approach to saturation (LAS):[64,65]

$$M = M_S\left[1 - \frac{a}{H} - \frac{b}{H^2}\right], \quad (4)$$

where the term a/H is connected to structural defects while the term b/H^2 to the magnetocrystalline anisotropy.

Zero-field-cooled–field-cooled (ZFC–FC) magnetizations were recorded within the 5–300 K temperature range under an applied magnetic field ($\mu_0 H_{app}$) of 2.5 mT using a Quantum Design PPMS magnetometer, equipped with a VSM head. The ZFC curve was recorded while heating the sample from 5 to 300 K in a magnetic field, after a preliminary cooling process under a zero magnetic field. The FC curve was obtained similarly but after cooling the sample in a 2.5-mT magnetic field. For magnetic measurements, the powder nanoparticles were immobilized using epoxy resin (sample-to-epoxy ratio was approximately 1:10) in gelatin capsules, to prevent any movement of the sample during the measurement. All the magnetic data were normalized by the total mass of the powder.

Results and discussion

To get insight into the sol–gel process, thermogravimetric analysis of the iron(III)-citrate xerogel (ICX) and citric acid (CA) for comparison, has been carried out in air and argon (**Figure** 2). The DT curve of CA exhibits a broad endothermic process with two steps near ~160°C and ~225°C, which could be attributed to the conversion of CA to aconitic acid ($C_6H_6O_6$, $-H_2O$) and itaconic acid ($C_5H_6O_4$, $-CO_2$) respectively.[62,66,67] At temperatures >400°C occurs the complete decomposition of the polymerized itaconic acid. However, the DT curves of the ICX, performed in oxygen and argon atmospheres for comparison, show a sharp exothermic peak centered in the same range (at ~192°C in oxygen and ~197°C in argon). The different decomposition temperatures between CA and ICX, as well as the different exo- and endothermic nature of the mass loss process, suggest a different thermal behavior due to the cross-linking process of the metal carboxylate complexes, bridged by ammonium ions.[45] A small difference in the residual mass between argon and air was observed; however, we refrain from further speculation, as variations in residual carbonaceous matter could lead to significant errors in estimation. Nonetheless, the overall thermal decomposition process appeared very similar under both atmospheres. This suggests that the auto-combustion process is driven by the decomposition of citrate and not by the atmospheric oxygen.[45] These

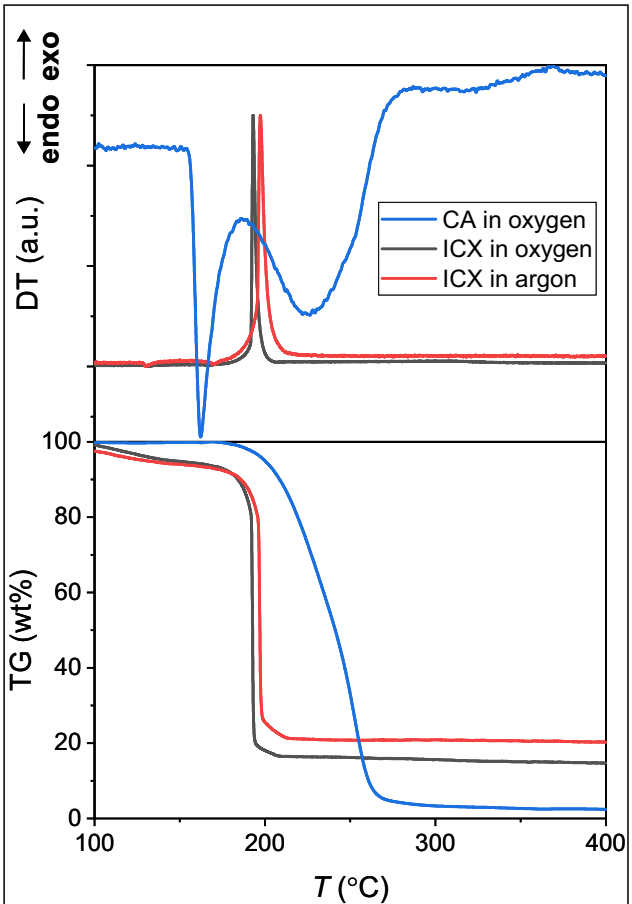

Figure 2. Differential thermal (DT) (upper panel) and thermogravimetric (TG) (bottom panel) curves of citric acid (CA) and iron(III)-citrate xerogel (ICX) in argon and oxygen atmospheres.

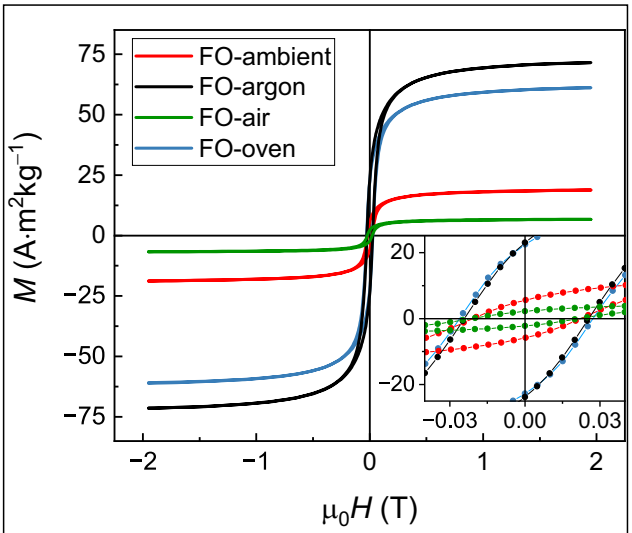

Figure 3. Field dependence of magnetization at 300 K of iron oxide nanoparticles prepared by sol–gel auto-combustion under different atmospheric conditions: ambient (air) atmosphere (red), argon flow (black), airflow (green), and tubular oven (air) (blue). The inset shows the low-field region of the magnetization curves.

results underscore the importance of investigating potential structural differences in the products synthesized under varying atmospheric conditions.

Combustion synthesis under different atmospheric conditions

Combustion in air (ambient conditions)

The combustion of gel performed in air, in an open beaker on a hot plate (ambient conditions), produces powders with large inhomogeneities and different colors, immediately noticeable to the naked eye, which belong to different phases of iron oxides (Supplementary information Figure S1a). The three-dimensional branched powders, achieved after the auto-combustion at 350°C (temperature of the surface of the hot plate, while local temperature of gel can differ), show a mixture of dark gray (associated with a high content of spinel phase) and orange/reddish areas (associated with the dominance of hematite).[25,68] The coexistence of Fe_3O_4/γ-Fe_2O_3 and α-Fe_2O_3 phases during combustion in air can be attributed to nonuniform temperature and oxygen distributions within the reactor.

The powders with different colors were qualitatively separated to conduct a preliminary investigation. The corresponding XRD patterns shown in Figure S1b, confirm that hematite, α-Fe_2O_3, with corundum structure, is the main crystalline phase in the orangish part (FO-orange), mostly located at the upper branches of the self-combusted tree. On the other hand, the gray powder (FO-dark) is mostly located at the bottom of the beaker and contains a significant amount of spinel phase, presumably mostly γ-Fe_2O_3. After grinding the whole product to reach a uniform system (FO-ambient), a mixture of α-Fe_2O_3 and γ-Fe_2O_3 was obtained as expected (Figure S1b).

The M_S values of these powders, estimated from the field-dependent magnetization loops at 300 K (Figure S2), show values corresponding to ~41 Am^2kg^{-1} for FO-dark, ~18 Am^2kg^{-1} for FO-ambient (see also **Figure** 3), and ~11 Am^2kg^{-1} for FO-orange. All of these values are lower than the bulk saturation magnetization of maghemite (~73 Am^2kg^{-1}),[7] but significantly higher than expected hematite (~0.5 Am^2kg^{-1}),[7] confirming the coexistence of the α-Fe_2O_3 and γ-Fe_2O_3 phases, as observed by XRD.

This experiment highlights that the SGAC process occurring in the uncontrolled air atmosphere is difficult to regulate due to the presence of several factors affecting the phase composition of the final product. The inhomogeneous temperature of the reaction (whose heating source is the hot plate) and the surrounding availability of environmental oxygen are parameters difficult to control in these experimental conditions. The combustion temperature of the ICX is near 200°C, as confirmed by TG/DT studies, but the applied temperature of the combustion (300–350°C) exceeds it. Moreover, the SGAC reaction is exothermic; thus, the local temperature of the as-burn powder can be significantly higher. In the presence of

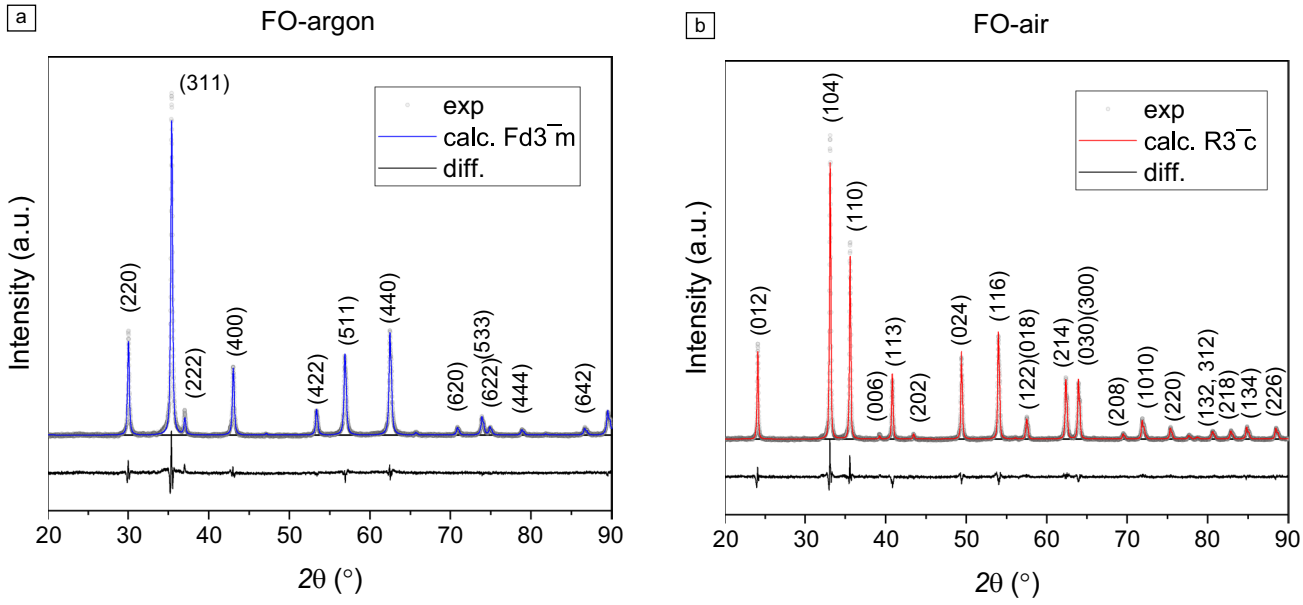

Figure 4. Rietveld refinement fits of the x-ray diffraction (XRD) patterns for (a) the sample prepared under a controlled argon atmosphere (FO-argon), composed mostly of magnetite, and (b) the sample prepared under airflow (FO-air), predominantly composed of hematite.

oxygen, it could induce the phase transformation from magnetite to maghemite, and then to hematite, following the route shown in Equation 1.

Combustion in controlled flow (Ar and air)

Performing the same reaction in a controlled inert atmosphere, we obtained single-phase iron oxide with a spinel structure and an average crystallite size of ~30 nm (**Figure** 4a). The XRD pattern matches the reference pattern for Fe_3O_4 (JCPDS No. 75–0033) with a measured lattice constant of 8.41(1) Å, which is very close to the bulk magnetite value of 8.40 Å.[7] This aligns with the results obtained earlier when performing combustion in an inert,[44] vacuum,[25] or oxygen-free atmosphere during synthesis.[57] The M_S value of the FO-argon sample, estimated by the hysteresis loop at 300 K (Figure 3), is ~74 Am^2kg^{-1}, which is lower than the bulk saturation magnetization of magnetite (91 Am^2kg^{-1}).[7] For Fe_3O_4 nanoparticles in the 20–30-nm range, $M_S \approx 60$ Am^2kg^{-1},[67] indicating that the value obtained in this work is consistent with those reported for particles of comparable crystallite size. This reduction is expected for nanoparticles and can be explained in terms of defects, symmetry breaking at the particle surface, and residual carbon impurities in the sample.[4,30,31,57,60] We note that this value is still significantly high and slightly higher than those values reported for Fe_3O_4 nanoparticles produced by a similar method in an oxygen-free environment.[57]

For comparison, the combustion of the ICX was performed in the same controlled way under airflow (FO-air). Figure 4b shows the corresponding XRD pattern: the dominant phase sample is α-Fe_2O_3 with an average $D_{XRD} = 41(4)$ nm, confirmed by XRD reflexes at 2θ = 24.1°, 33.1°, 35.7°, 40.9°, 49.4°, 54.1°, 57.7°, 62.5°, and 64.0°, related to (012), (104), (110), (113), (024), (116), (018), (214), and (300) planes (JCPDS No. 33–0664). However, at the nanoscale, the broadening of diffraction peaks makes the analysis even more complicated; thus, one cannot exclude that the possible content of the spinel phase is below the detection limit of the laboratory XRD setup (<3 wt%). While the presence of the spinel phase was not detected even after performing Rietveld analysis, we note that the most intense reflection signal (311) of maghemite has a scattering angle almost identical to the reflection (110) of hematite, and most of the other reflections are in superposition.[15] The formation of hematite can be promoted by increasing the reaction temperature, tuning the partial pressure of inert gases, or modifying other synthesis parameters such as the fuel-to-oxidizer ratio and heating rate.[44,45,70] These factors influence both the local oxygen availability and the duration of the high-temperature stage, which together govern the extent of the $Fe_3O_4 \rightarrow \gamma\text{-}Fe_2O_3 \rightarrow \alpha\text{-}Fe_2O_3$ transformation.

Interestingly, the magnetization loop at 300 K of the FO-air sample (Figure 3) shows significantly high an $M_S \approx 7$ Am^2kg^{-1} and $\mu_0 H_C \approx 22$ mT, even though the XRD pattern corresponds to the hematite phase. Cannas et al.[45] suggested that the presence of some residual γ-Fe_2O_3 can be responsible for the high magnetization of some hematite samples, in opposite to observed in smaller hematite crystals caused by the surface's uncompensated spins.[71] As a matter of fact, the coercivity of the FO-air sample matches very well with the FO-ambient sample, despite significantly different values of M_S. This supports the hypothesis of having a residual spinel phase as the main contribution to magnetization.

Combustion in tubular oven (air)

Although TG analysis of ICX in argon and air showed no significant differences in the auto-combustion process, the structure and magnetic properties of the resulting powders are drastically different. This suggests that the post-synthesis exposure to the atmosphere plays a key role in modifying the as-burnt powders. To investigate this effect further, an additional sample was synthesized using a tubular oven without active atmosphere control, but in a configuration where the likelihood of atmospheric oxygen interacting with the as-burned material was reduced due to the sample remaining in the gaseous products of the SGAC reaction during cooling.

The combustion of ICX inside the tubular allows for obtaining powders composed mainly of the spinel ferrite phase (Figure S3). The observed XRD reflections at $2\theta = 30.3°$, 35.6°, 43.5°, 54.1°, 57.6°, and 62.5° are related to (220), (311), (400), (422), (511), and (440) planes, respectively, corresponding to γ-Fe_2O_3 (JCPDS No. 39–1346). However, the XRD pattern of the FO-oven sample exhibits two notable differences compared to that of FO-argon: (1) the presence of additional reflections with a low intensity attributed to lower symmetry of the superstructure owing to the ordering of oxygen vacancies, typical of maghemite;[22] (2) a slight shift in the positions of the main reflections, suggesting a different lattice parameter. The calculated lattice parameter for FO-oven is 8.32(2) Å, closely matching the value reported for bulk maghemite (8.34 Å).[7] Correspondingly, the saturation magnetization (M_S) of FO-oven (~63 Am^2kg^{-1}, Figure 3) is slightly lower than that observed for the Fe_3O_4-rich FO-argon sample.

Additionally, we performed TG analysis of FO-argon and FO-oven samples (Figure S4). As expected, the heating of the FO-oven sample leads to the burning of some residual organics (~18 wt%) and, thus, corresponding mass loss. The mass loss process of the FO-argon sample overlaps with a mass gain due to the oxidation of Fe_3O_4 to Fe_2O_3.[72] Theoretically, the full oxidation of magnetite to maghemite adds about a 3.45 wt% in the solid due to the extra oxygen (Equation 1).[73] We performed the semi-qualitative deconvolution of TG curve into two processes: (1) burning of residual organic matter and (2) oxidation of Fe_3O_4 to Fe_2O_3 (Figure S4). The second process saturates at 350(20)°C, which aligns well with expectations.[23] As well, the obtained mass gain estimated with consideration of organic content of 10 wt% was 3.4(5) wt%, again close to theoretical, considering full oxidation of Fe_3O_4 to Fe_2O_3.

According to previous studies,[44,57] the combustion of iron-citrate gels in an oxygen-free atmosphere proceeds through the initial formation of Fe_3O_4, which can be subsequently oxidized to γ-Fe_2O_3 or α-Fe_2O_3 depending on oxygen availability and temperature. Consistent with this mechanism, our results indicate that synthesis under argon resulted in the formation of the Fe_3O_4 phase, while the same reaction an oven in air favors the formation of γ-Fe_2O_3. Presumably, the oxygen content in oven is sufficient to oxidize Fe_3O_4 to γ-Fe_2O_3, but not high enough to accelerate combustion and drive the transformation to α-Fe_2O_3. The less controlled heating on a hot plate results in partial conversion to α-Fe_2O_3 due to local overheating. The subproducts of the reaction (carbonaceous residues and released gases) could also play an important role in stabilizing the final product of the reaction.[45]

Maghemite and magnetite: Magnetic structure and magnetic properties

To gain deeper insight into the impact of phase composition on magnetic properties, this section presents a comparative analysis of two representative samples: (1) FO-argon, predominantly composed of magnetite, and (2) FO-oven, enriched in maghemite. These serve as model systems for evaluating the characteristic magnetic responses of Fe_3O_4 and γ-Fe_2O_3 phases, respectively. As expected for combustion-based synthesis routes, the obtained iron oxide powders consist of dense aggregates of irregularly shaped particles, typical of materials produced through rapid self-propagating combustion reactions.[42,74] The TEM images (Figure S5) reveal that these aggregates are composed of nanocrystalline domains with sizes of few tens of nanometers, consistent with the spinel structure identified by XRD. The individual crystallites are clearly distinguishable, confirming the nanocrystalline nature of both the magnetite-rich FO-argon and maghemite-rich FO-oven samples. Despite the overall dense and agglomerated morphology, the particle sizes observed by TEM are comparable to those estimated from XRD analysis ($D_{XRD} \approx$ 20 nm and $D_{XRD} \approx 30$ nm for FO-oven and FO-argon samples, respectively). Notably, these crystallite sizes lie well below the single-domain critical size for magnetite (~80 nm[7,69]), suggesting that their magnetic behavior is predominantly governed by single-domain characteristics.

Field-dependent magnetization loops at 300 K reveal minimal differences between the FO-argon and FO-oven samples (Figure 3). The M_S of Fe_3O_4 is known to be slightly higher than that of γ-Fe_2O_3[7,8,26] accordingly, the FO-argon sample exhibits an ~15% higher M_S compared to the FO-oven sample. However, this difference could also arise from surface effects and structural defects in the nanoparticles, which make direct comparison with bulk analogs less straightforward. The FO-argon sample also shows slightly lower coercivity and remanence ratio (FO-argon: $\mu_0 H_C \approx 24$ mT, $M_R/M_S \approx 0.31$; FO-oven: $\mu_0 H_C \approx 26$ mT, $M_R/M_S \approx 0.35$).

The high content of stoichiometric magnetite in the FO-argon sample is further supported by the temperature dependence of magnetization (**Figure** 5a). Both $M_{ZFC}(T)$ and $M_{FC}(T)$ curves exhibit a pronounced kink, corresponding to the well-known Verwey transition, associated with charge ordering of Fe^{2+} and Fe^{3+} ions at octahedral sites, which is characteristic of magnetite.[30,75] The position of the peak of the first derivative of the difference between these two branches, $T_V \approx 117$ K, matches the temperature of the Verwey transition for bulk magnetite.[61] The second peak that appears at higher temperatures ($T_P = 230$–240 K) is likely due to the approach to the superparamagnetic state. It is evident

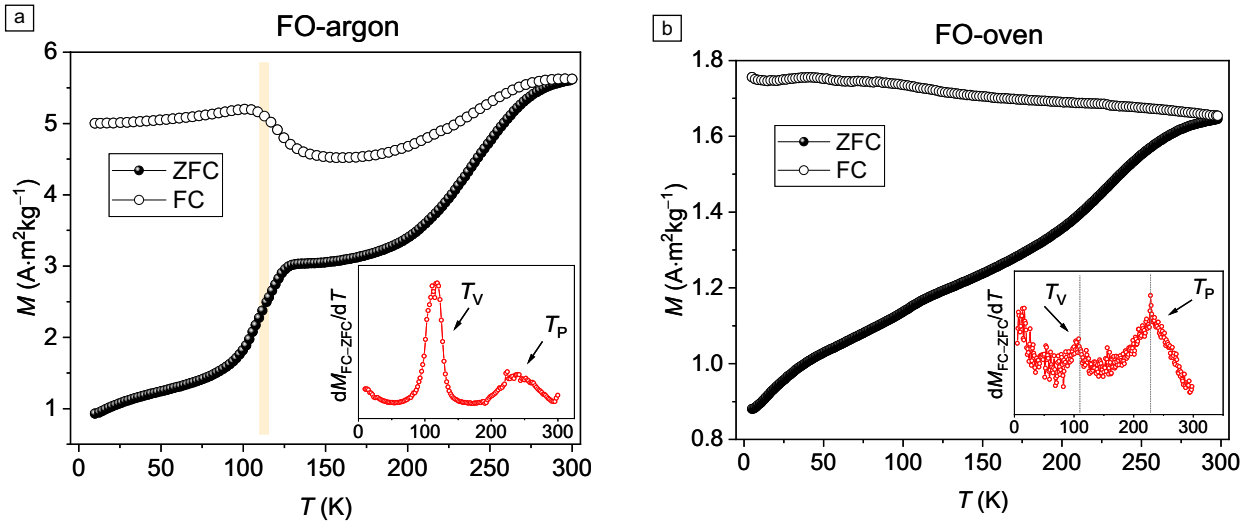

Figure 5. Zero-field-cooled (ZFC) and field-cooled (FC) magnetization curves of (a) the magnetite-rich FO-argon sample and (b) the maghemite-rich FO-oven sample, measured as a function of temperature. The insets show the first derivative with respect to temperature of the difference between the FC and ZFC magnetizations, $dM_{FC-ZFC}(T)/dT$.

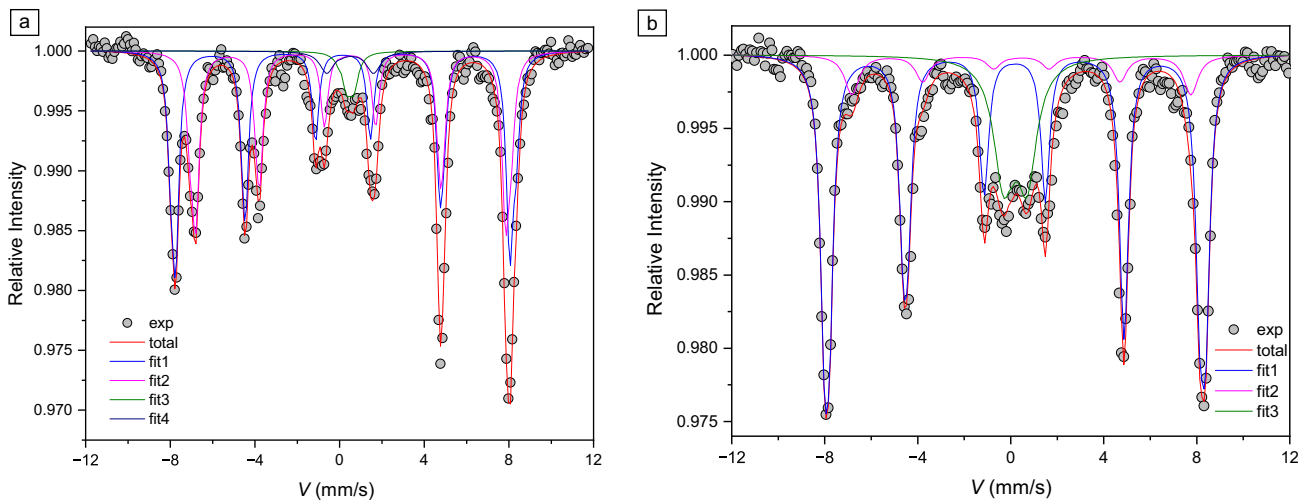

Figure 6. Mössbauer spectra of FO-argon (a) and FO-oven (b) at 300 K.

from the smooth shape of the ZFC–FC curve of the FO-oven sample (Figure 5b) that, although a peak near T_V appeared in the $dM_{FC-ZFC}(T)/dT$, its intensity is much lower compared to that appearing in the FO-argon sample, indicating the lower content of magnetite.

To probe the local cationic structure, ^{57}Fe Mössbauer spectra were recorded for the FO-argon and FO-oven samples at 300 K (**Figure** 6). For the FO-argon sample (Figure 6a), the spectrum shows a pronounced magnetic hyperfine splitting with minor superparamagnetic contributions (8%). The spectrum was fitted using two magnetic sextets, attributed to Fe^{3+} ions in tetrahedral A-sites and Fe^{2+}/Fe^{3+} ions in octahedral B-sites of Fe_3O_4 (**Table** I), suggesting no secondary phases. Typically for stoichiometric magnetite, the area ratio S_A/S_B of 0.5 corresponds to full electron exchange between Fe^{2+} and Fe^{3+} in B-sites T_V.[76] However, the observed ratio $S_A/S_B = 1.14$ suggests deviations from stoichiometry, likely arising from the presence of maghemite phase, as suggested by the mean value of isomer shift $\langle\delta\rangle = 0.49$ (24% maghemite/76% magnetite). In contrast, the FO-oven sample at 300 K (Figure 6b) shows a single broad and asymmetric sextet, typical of maghemite, where Fe^{3+} ions occupy both A and B sites with similar hyperfine fields.[52] The absence of distinguishable features for Fe^{2+} and the overlapping site contributions reflect the more disordered nature of γ-Fe_2O_3, as expected from the synthesis route in an oxidizing atmosphere. The mean value of isomer

Table I. Hyperfine parameters estimated from the ^{57}Fe Mössbauer spectra at $T = 300$ K: isomer shift/quadrupolar separation ($\delta/\Delta E_Q$), quadrupole shift (ε), magnetic hyperfine field (B_{hyp}), and area of the spectrum component (S).

Sample	Component	$\delta/\Delta E_Q$ (mm/s)	2ε (mm/s)	B_{hyp} (T)	S (%)
FO-argon	Fit1 (Fe^{3+}_A)	0.32	−0.02	51.3	49
	Fit2 ($Fe^{3+/2+}$_A)	0.66	0.03	45.7	43
	Fit3 (doublet)	0.61	0.35	0	4
	Fit4 (doublet)	0.66	2.11	0	4
FO-oven	Fit1 (sextets)	0.33	−0.04	50.0	69
	Fit2 (sextets)	0.62	0.0	45.0	10
	Fit3 (doublet)	0.35	0.92	0	21

shift$\langle\delta\rangle = 0.36$ corresponds to maghemite with only a very small percentage of partial electronic charge transfer from Fe^{3+} to Fe^{2+}.[60]

Oxidation process and evolution of magnetic properties

Experimental evidence discussed in the previous paragraphs indicates that the combustion environment plays a crucial role in determining the phase composition and magnetic properties of the synthesized iron oxide nanoparticles. Performing combustion in an inert argon atmosphere favors the formation of almost stoichiometric Fe_3O_4 with higher M_S and a clear Verwey transition, while combustion in air, either in a controlled way or in the tubular oven, leads to predominant oxidation and the formation of γ-Fe_2O_3.

To better investigate the processes causing the transformation of iron oxide phases, postannealing of FO-ambient samples was performed in an air atmosphere. **Figure** 7 shows the variations of XRD patterns of powder subjected to treatment at different temperatures. The FO-ambient sample was mostly composed of α-Fe_2O_3 with a small trace of γ-Fe_2O_3 (minor Fe_3O_4 content cannot be excluded). The fingerprint (220) and (440) reflections of the spinel phase are weak and almost disappear when the temperature exceeds 500°C.[25] This observation is consistent with previous studies on annealed γ-Fe_2O_3 particles of comparable crystallite sizes, which demonstrated that in samples with both α- and γ-Fe_2O_3, the transition to a single-phase α-Fe_2O_3 occurs upon annealing at temperatures above 500°C.[77]

To gain deeper insight into the transformation process from the spinel phase, an *in situ* XRD analysis was performed during the thermal treatment of magnetite-rich FO-argon samples in air (Figure S6). The results confirm that the transformation of Fe_3O_4 to α-Fe_2O_3 occurs via an intermediate γ-Fe_2O_3 phase.[25,29] Maghemite starts to form already at 200°C, as shown by the weak reflections at low angles, while hematite appears at 400°C, and becomes the dominant phase above 500°C. At this point, we should note that the pattern of the as-burnt FO-ambient sample is almost identical to that of the FO-air sample when annealed at 400°C, both composed

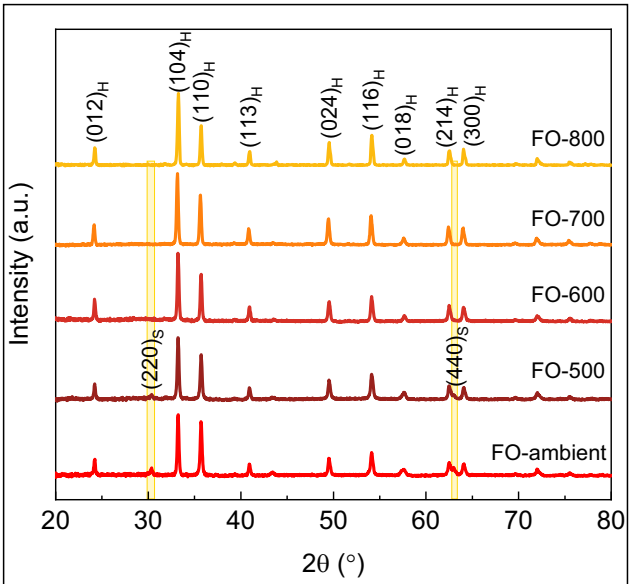

Figure 7. X-ray diffraction patterns of the as-burnt FO-ambient sample and the same powder after thermal treatment in air for 1 h at temperatures ranging from 500°C to 800°C. The diffraction peaks corresponding to the spinel phase are labeled with "S" and those corresponding to the hematite phase are labeled with "H." The yellow areas highlight the positions of the characteristic peaks for the spinel phase.

of a mixture of α-Fe_2O_3 and γ-Fe_2O_3 phases. This suggests that the starting Fe_3O_4 could transform into this mixture if the as-burnt powder is exposed to air at a temperature near 400°C.

Consistently, the magnetic properties also change upon changing the temperature of annealing; specifically, the M_S is reduced from ~17 to ~0.5 Am^2kg^{-1} when comparing the as-burnt FO-ambient sample to samples annealed for 1 h in an ambient atmosphere (**Figure** 8a). While the presence of spinel ferrite is almost undetectable by XRD in samples annealed at temperatures above 500°C, the M_S remains much higher than expected for pure hematite. For example, the M_S value for the FO-500 sample is ~14 Am^2kg^{-1}, and for the FO-600 sample, it is ~2 Am^2kg^{-1}. A closer view of the hysteresis loops of the sample treated at 700°C is shown in Figure 8b, revealing the presence of two magnetic phases by characteristic kinks in hysteresis loops and two peaks in their derivatives (inset of Figure 8b).[78,79] However, the sample treated at 800°C is a single-phase α-Fe_2O_3 characterized by a smooth hysteresis with the M_S value similar to the bulk analogue and coercivity field (~0.35 T) exceeding those of spinel oxide nanoparticles more than an order of magnitude.

Assuming that the magnetic hysteresis of a bi-magnetic system can be represented as a superposition of the magnetizations of the individual phases and considering negligible magnetic interactions between them, we determined the mass fractions of the two phases, denoted as ϕ_H for α-Fe_2O_3 and ϕ_M for γ-Fe_2O_3,

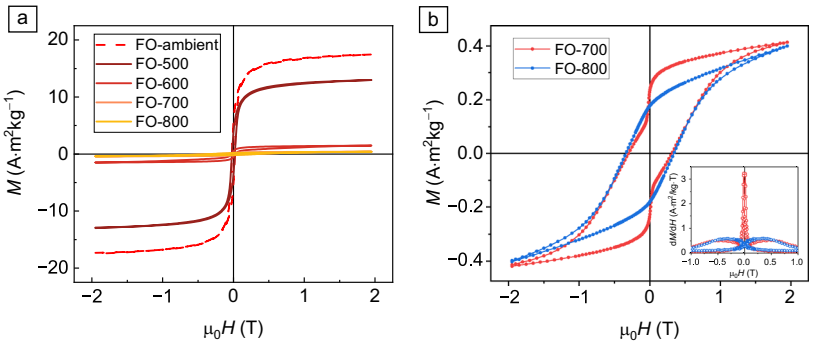

Figure 8. (a) Field dependence of magnetization of the FO-ambient sample in the as-burnt state and after thermal treatment in air for 1 h at temperatures from 500°C to 800°C. (b) Enlarged view of the hysteresis loops for the samples treated at 700°C and 800°C; the inset shows the derivative *dM*/*dH* versus *H*. All measurements were performed at 300 K.

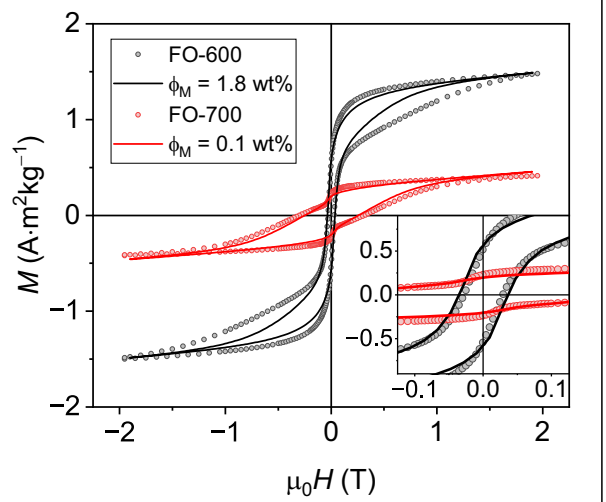

Figure 9. Measured hysteresis loops at 300 K for the FO-600 and FO-700 samples (symbols) and simulated hysteresis loops obtained by the superposition of the maghemite and hematite hysteresis loops (lines). The mass fraction of maghemite (ϕ_M) used in the simulations is indicated.

where $\phi_H + \phi_M = 1$. The total magnetization, M_{total}, was computed as:

$$M_{\text{total}} = M_H(1 - \phi_M) + M_M\phi_M, \quad (5)$$

where M_H and M_M represent the magnetization of the hematite and maghemite phases, respectively. The loops of FO-800 and FO-oven samples were used as references for the $M(H)$ functions of α-Fe_2O_3 and γ-Fe_2O_3, respectively. The superposition results were then used to simulate the magnetic behavior of samples containing both iron oxide phases, keeping the low content of γ-Fe_2O_3 (**Figure** 9). Considering that the magnetization of γ-Fe_2O_3 is two orders of magnitude higher than that of α-Fe_2O_3 when the relative mass fraction of γ-Fe_2O_3 to α-Fe_2O_3 is around 1 wt%, the magnetic moments of both phases become comparable. This results in a characteristic bimodal hysteresis loop (Figure 9).[80] The good agreement obtained by following the superposition rule and the preservation of switching fields (inset of Figure 8b) suggest that the magnetic coupling between the two phases is rather weak.[79]

This approach allowed estimating the magnetic iron oxide content in samples where it coexists with hematite. For example, in the FO-ambient sample, the estimated ϕ_M is approximately 30 wt% and is reduced to 20 wt% when annealed at 500°C. This content is slightly higher than the spinel phase content estimated from XRD—19 wt% and 13 wt%, respectively. However, interestingly, with such an analysis of magnetic hysteresis loops, we can gain insight into systems with small amounts of spinel phases that are below the detection limit of XRD. In this way, we determined ϕ_M to be ~1.8 wt% and 0.1 wt% in samples FO-600 and FO-700, respectively.

Scale-up and reproducibility of the synthesis in Ar

The scale-up and reproducibility of the combustion in Ar were evaluated with the aim of demonstrating that it can produce uniform iron oxide nanoparticles with consistent structural and magnetic properties across multiple batches. For that purpose, 19 additional batches of iron oxide nanoparticles were synthesized under the same conditions (i.e., controlled argon atmosphere), and structural and magnetic characterization were performed for each sample in order to evaluate the reproducibility of the synthesis. Based on the XRD patterns (**Figure** 10a), all samples exhibited a cubic spinel structure with no detectable impurities (e.g., hematite). As shown in Figure 10b, the D_{XRD} was calculated for each sample, comparing the average over the six most intense reflections with that from the (440) reflection only, which is less affected by instrumental broadening. The average D_{XRD} across all samples was 29(2) nm when averaged over multiple reflections, while that determined from the (440) reflection was 25(1) nm. The variations in D_{XRD} between samples detected by both approaches were 7% and 5% for the averaged value and that calculated for (440) reflection, respectively. The apparent error indicated for each sample calculated from averaging of all intense reflections primarily reflects differences in peak fitting precision at low 2θ angles and possible preferred orientation effects during crystal growth. When the crystallite size is estimated using the high-angle (440) reflection, the results are more consistent (standard deviation ≈1 nm), confirming that the crystalline sizes are uniform across the studied series.

The lattice parameter *a* was calculated for each sample using the Equation 3 and is shown in Figure 10c. The values range between 8.394 Å and 8.423 Å, with an overall average of

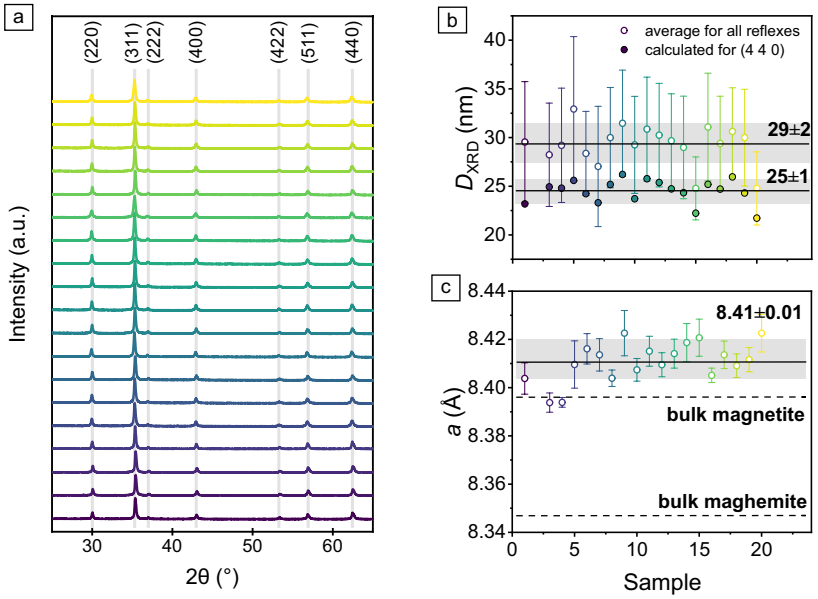

Figure 10. (a) X-ray diffraction (XRD) patterns of 19 iron oxide nanoparticle samples prepared by sol–gel auto-combustion in Ar; (b) the crystallite size D_{XRD} calculated using the Scherrer equation, averaged across all reflections (open circles) and for the (440) reflection (solid circles); (c)lLattice parameter *a*; values for bulk maghemite (8.34 Å) and magnetite (8.40 Å) shown by dashed lines. For D_{XRD} and *a* obtained from the averaging of six reflexes, the error bars demonstrating standard deviations (SD) are rendered by mustaches. Averaged values over 19 samples and SD are shown by a solid horizontal line and gray area, respectively.

8.41(1) Å across the 19 samples. The measured lattice parameter is close to the value for bulk magnetite (8.40 Å),[7] confirming the expected selective phase. Although these values are generally consistent with bulk lattice constants within experimental error, lattice parameters in nanoparticles are often slightly expanded, likely due to the presence of structural defects.

Room-temperature field-dependent magnetization measurements were also performed (**Figure** 11a). The M_S values are lower than the saturation magnetization of bulk magnetite (91 Am^2kg^{-1} at 300 K),[7] with an average M_S of 70(7) Am^2kg^{-1}. This reduction is expected due to key factors, such as particle size effects, surface disorder, and residual impurities. Figure 11a shows that, for each sample, the magnetizations measured at the maximum applied field of 2 T and those obtained after fitting with Equation 4 are in good agreement, confirming that the samples are saturated at 2 T. On the

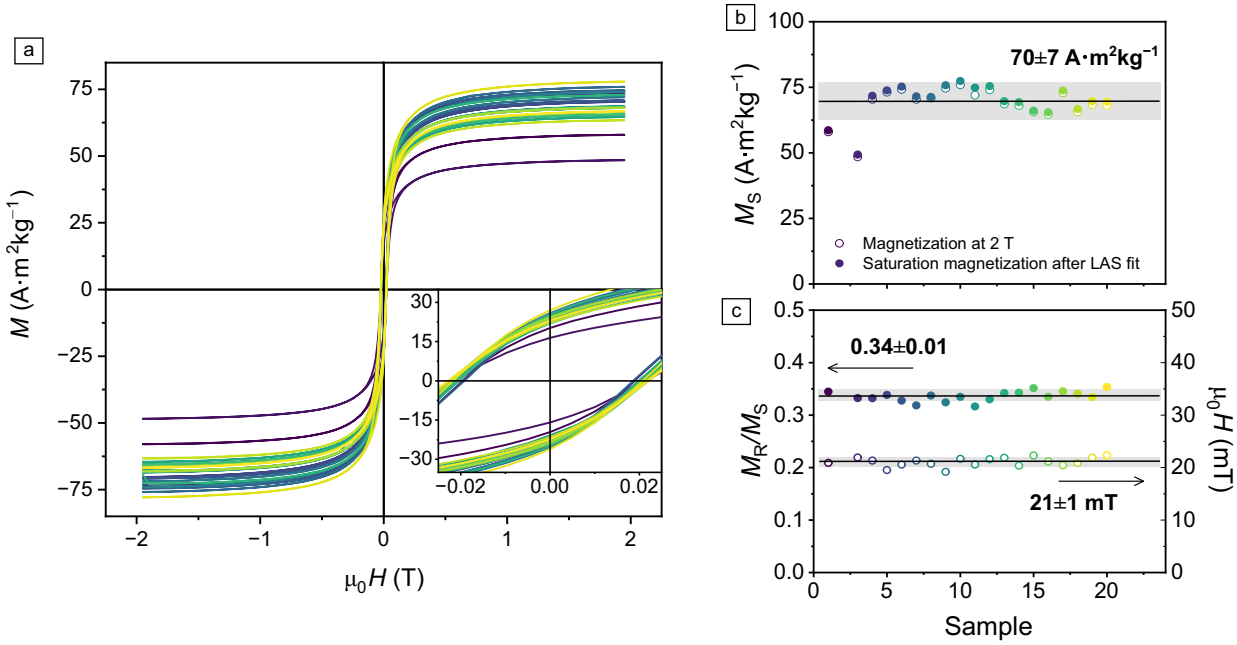

Figure 11. (a) *M–H* hysteresis loops of 19 iron oxide nanoparticle samples prepared by sol–gel auto-combustion in atmosphere, with the inset showing the low-field region; (b) saturation magnetization M_S calculated at 2 T (empty symbols) and from the law of approach to saturation (LAS) fit (solid symbols); (c) remanence-to-saturation magnetization ratio M_R/M_S (solid symbols) and coercivity $\mu_0 H_C$ (empty symbols) for each sample. Averaged values over 19 samples and standard deviation are shown by a solid horizontal line and gray area, respectively. All measurements were performed at 300 K.

other hand, the M_R/M_S and $\mu_0 H_C$ for each sample (Figure 11b) are consistent across all batches, confirming that the reported procedure under the argon flow can be used to synthesize nanoparticles with reproducible structural and magnetic properties.

Conclusion

Controlling the combustion atmosphere is crucial for the phase-selective synthesis of iron oxide nanoparticles. Performing sol–gel combustion under an argon atmosphere enables the production of nanoparticles with a dominant Fe_3O_4 phase, exhibiting the highest saturation magnetization (~74 Am^2/kg^{-1} at 300 K), compared to samples synthesized under other conditions, and a distinct Verwey transition. Mössbauer spectroscopy confirmed that synthesis under an argon atmosphere yields nanoparticles with a dominant Fe_3O_4 phase, evidenced by distinct Fe^{2+}/Fe^{3+} site contributions and an average isomer shift consistent with a magnetite content of ~76 wt.%. The scalability and reproducibility of the synthesis in argon were validated by successfully synthesizing 20 consistent batches under argon flow, producing samples with reproducible magnetic properties.

When synthesis was performed in a tubular oven, where the access of oxygen is limited by the lack of recirculation of air, the product was mostly γ-Fe_2O_3 with moderate magnetic properties. In contrast, synthesis in an ambient air environment led to mixed α-/γ-Fe_2O_3 phase products with inferior magnetic characteristics. Additionally, thermal treatment studies elucidated the phase transformation pathway from Fe_3O_4 to α-Fe_2O_3 via a γ-Fe_2O_3 intermediate in the temperature range of 200–500°C, with single-phase α-Fe_2O_3 forming only at 800°C. This work provides a clear strategy for producing phase-controlled iron oxide nanoparticles and underscores the critical impact of atmospheric conditions on nanoparticle synthesis.

These results highlight the sensitive balance between oxygen availability and local temperature during gel combustion. Even minor variations in the atmospheric composition or heating conditions lead to significant changes in phase composition and magnetic response. Although the present work has focused on synthesis in argon, future studies will systematically investigate other inert or controlled-oxidation atmospheres (e.g., nitrogen, mixed Ar/O_2) and reaction regimes, including self-propagating combustion, to further clarify the mechanism of phase formation and improve control over nanoparticle microstructure and magnetic properties. A detailed investigation of the individual steps involved in the combustion process is crucial for achieving precise control over the phase composition of the resulting products and therefore warrants further study.

Author contributions

J.P.M.M.: data curation; investigation; methodology; writing—original draft. M.A.: conceptualization; data curation; formal analysis; investigation; methodology; writing—original draft. N.Y.: data curation; investigation; validation; writing—original draft; writing—review and editing. F.T.S.: investigation; methodology. G.B.: formal analysis; investigation; methodology; supervision; validation; writing—review and editing. G.V.: data curation; formal analysis; project administration; resources; supervision; validation; writing—review and editing. A.G.H.: investigation; methodology. A.R.: investigation; methodology. E.S.: investigation; methodology. S.A.: formal analysis; project administration; resources; supervision; validation; writing—review and editing. S.S.: investigation; writing—original draft. P.Man.: investigation; methodology; supervision. P.Mal.: data curation; formal analysis; investigation; methodology; validation; writing—original draft; writing—review and editing. D.P.: conceptualization; data curation; formal analysis; funding acquisition; methodology; project administration; resources; supervision; validation; writing—review and editing.

Funding

Open access funding provided by Università degli Studi di Genova within the CRUI-CARE Agreement. The authors acknowledge the support from Project code PE0000021, Concession Decree No. 1561 of 11.10.2022 adopted by "Ministero dell'Università e della Ricerca (MUR)," according to attachment E of Decree No. 1561/2022, Project title "Network 4 Energy Sustainable Transition-NEST."

Data availability

The data that support the findings of this study are available from the corresponding author upon reasonable request.

Competing interests

The authors have no conflict to disclose.

Supplementary Information

The online version contains supplementary material available at https://doi.org/10.1557/s43577-025-01045-z.

Open Access

References

1. M. Liu, Y. Ye, J. Ye, T. Gao, D.Wang. G. Chen, Z. Song, *Magnetochemistry* **9**(4), 110 (2023). https://doi.org/10.3390/magnetochemistry9040110
2. R. Ding, C. Guida, C.L. Pearce, E. Arenholz, J.-M. Grenèche, A. Gloter, A.C. Scheinost, K.O. Kvashnina, K. Wang, A. Fernandez-Martinez, Y. Mu, K.M. Rosso, L. Charlet, *Sci. Adv.* **11**(2), eadq3650 (2025). https://doi.org/10.1126/sciadv.adq3650

3. T. Kim, S. Sim, S. Lim, M.A. Patino, J. Hong, J. Lee, T. Hyeon, Y. Shimakawa, S. Lee. J.P. Attfield, J.-G. Park, *Nat. Commun.* **12**, 6356 (2021). https://doi.org/10.1038/s41467-021-26566-4
4. G.C. Lavorato, A.A. de Almeida, C. Vericat, M.H. Fonticelli, *Nanotechnology* **34**(19), 192001 (2023). https://doi.org/10.1088/1361-6528/acb943
5. J.M.D. Coey, M. Venkatesan, H. Xu, "Introduction to Magnetic Oxides," in *Functional Metal Oxides: New Science and Novel Applications*, ed. by S.B. Ogale, T.V. Venkatesan, M.G. Blamire (Wiley-VCH Weinheim, 2013), chap. 1, pp. 1–49
6. P.P. Falciglia, E. Gagliano, P. Scandura, C. Bianco, T. Tosco, R. Sethi, G. Varvaro, E. Agostinelli, C. Bongiorno, A. Russo, S. Romano, G. Malandrino, P. Roccaro, F.G.A. Vagliasindi, *Sep. Purif. Technol.* **296**, 121342 (2022)
7. J.M.D. Coey, *Magnetism and Magnetic Materials* (Cambridge University Press, Cambridge, 2010)
8. G. Varvaro, A. Omelyanchik, D. Peddis, "Ferroic Transition Metal Oxide Nano-heterostructures: From Fundamentals to Applications," in *Tailored Functional Oxide Nanomaterials: From Design to Multi-Purpose Applications*, ed. by C. Maccato, D. Barreca (Wiley, Weinheim, 2022), pp. 405–437
9. E.M. Múzquiz-Ramos, V. Guerrero-Chávez, B.I. Macías-Martínez, C.M. López-Badillo, L.A. García-Cerda, *Ceram. Int.* **41**, 397 (2015)
10. Y. Bao, J.A. Sherwood, Z. Sun, *J. Mater. Chem. C* **6**, 1280 (2018)
11. E.A. Kuchma, P.V. Zolotukhin, A.A. Belanova, M.A. Soldatov, T.A. Lastovina, S.P. Kubrin, A.V. Nikolsky, L.I. Mirmikova, A.V. Soldatov, *Int. J. Nanomed.* **12**, 6365 (2017)
12. M. Sainz-Menchón, I. González de Arrieta, T. Echániz, K. Nader, M. Insausti, A. Canizarès, O. Rozenbaum, G.A. López, *Phys. Chem. Chem. Phys.* **27**, 8498 (2025)
13. G.F. Dionne, *Magnetic Oxides*, 1st edn. (Springer, Boston, 2009)
14. L. Suber, P. Imperatori, A. Mari, G. Marchegiani, M.V. Mansilla, D. Fiorani, W.R. Plunkett, D. Rinaldi, C. Cannas, G. Ennas, D. Peddis, *Phys. Chem. Chem. Phys.* **12**, 6984 (2010)
15. P. Maltoni, G. Varvaro, N. Yaacoub, G. Barucca, J.P. Miranda-Murillo, J. Tirabzonlu, S. Laureti, D. Fiorani, R. Mathieu, A. Omelyanchik, D. Peddis, *J. Phys. Chem. C* **129**(1), 591 (2024). https://doi.org/10.1021/acs.jpcc.4c05320
16. R. Ilmetov, *Mater. Today Proc.* **6**, 11 (2019)
17. N. Basavegowda, K. Mishra, Y.R. Lee, *Adv. Nat. Sci. Nanosci. Nanotechnol.* **8**(2), 025017 (2017)
18. Y. Zheng, Y. Cheng, Y. Wang, F. Bao, L. Zhou, X. Wei, Y. Zhang, Q. Zheng, *J. Phys. Chem. B* **110**, 3093 (2006)
19. M.R. Tohidifar, E. Taheri-Nassaj, P. Alizadeh, *Mater. Chem. Phys.* **109**, 137 (2008)
20. Y. Zhang, H. Ye, H. Liu, K. Han, *Powder Technol.* **229**, 206 (2012)
21. A. Mirzaei, S.G. Leonardi, G. Neri, *Ceram. Int.* **42**, 15119 (2016)
22. H.L. Andersen, B.A. Frandsen, H.P. Gunnlaugsson, M.R.V. Jørgensen, S.J.L. Billinge, K.M.Ø. Jensen, M. Christensen, *IUCrJ* **8**, 33 (2021)
23. F. Bourgeois, P. Gergaud, H. Renevier, C. Leclere, G. Feuillet, *J. Appl. Phys.* **113**, 013510 (2013). https://doi.org/10.1063/1.4772714
24. Z. Li, C. Chanéac, G. Berger, S. Delaunay, A. Graff, G. Lefèvre, *RSC Adv.* **9**, 33633 (2019)
25. J. Xu, H. Yang, W. Fu, K. Du, Y. Sui, J. Chen, Y. Zeng, M. Li, G. Zou, *J. Magn. Magn. Mater.* **309**, 307 (2007)
26. Y. El Mendili, J.-F. Bardeau, N. Randrianantoandro, F. Grasset, J.-M. Greneche, *J. Phys. Chem. C* **116**, 23785 (2012)
27. T.J. Daou, G. Pourroy, S. Bégin-Colin, J.M. Grenèche, C. Ulhaq-Bouillet, P. Legaré, P. Bernhardt, C. Leuvrey, G. Rogez, *Chem. Mater.* **18**, 4399 (2006)
28. R. Ding, C. Guida, C. I. Pearce, E. Arenholz, J.-M. Grenèche, A. Gloter, A.C. Scheinost, K.O. Kvashnina, K. Wang, A. Fernandez-Martinez, Y. Mu, K.M. Rosso, L. Charlet, *Sci. Adv.* **11**(20), eadq3650 (2025)
29. A. Cervellino, R. Frison, G. Cernuto, A. Guagliardi, N. Masciocchi, *J. Appl. Crystallogr.* **47**, 1755 (2014)
30. D. González-Alonso, J. I. Espeso, H. Gavilán, L. Zeng, M. T. Fernandez-Diaz, G. Subías, I. de Pedro, J. Rogriguez, P. Bender, L. Fernandez Barquin, C. Johansson, *Nanoscale Adv.* **3**, 1 (2021)
31. J. Santoyo Salazar, L. Perez, O. De Abril, L. Truong Phuoc, D. Ihiawakrim, M. Vazquez, J.M. Greneche, S. Begin-Colin, G. Pourroy, *Chem. Mater.* **23**(6), 1379 (2011)
32. T. Kim, S. Sim, S. Lim, M.A. Patino, J. Hong, J. Lee, T. Hyeon, Y. Shimakawa, S. Lee, J.P. Attfield, J.G. Park, *Nat. Commun.* **12**, 10 (2021)
33. H. Jung, A.M. Schimpf, *Nanoscale* **13**, 17465 (2021)
34. H. Sharifi Dehsari, V. Ksenofontov, A. Möller, G. Jakob, K. Asadi, *J. Phys. Chem. C* **122**(49), 28292 (2018)
35. M. Testa Anta, M.A. Ramos-Docampo, M. Comesaña-Hermo, B. Rivas-Murias, V. Salgueiriño, *Nanoscale Adv.* **1**(6), 2086 (2019). https://doi.org/10.1039/C9NA00064J
36. C.R. Vestal, Z.J. Zhang, *Int. J. Nanotechnol.* **1**, 240 (2004)
37. B. Aslibeiki, P. Kameli, I. Manouchehri, H. Salamati, *Curr. Appl. Phys.* **12**, 812 (2012)
38. M.D. Nguyen, L. Deng, J.M. Lee, K.M. Resendez, M. Fuller, S. Hoijang, F. Robles-Hernandez, C. Chu, D. Litvinov, V.G. Hadjiev, S. Xu, M. Phan, T.R. Lee, *Small* **20**, 1 (2024)
39. G. Hemery, A.C. Keyes, E. Garaio, I. Rodrigo, J.A. Garcia, F. Plazaola, E. Garanger, O. Sandre, *Inorg. Chem.* **56**, 8232 (2017)
40. H. Gavilán, G.M.R.R. Rizzo, N. Silvestri, B.T. Mai, T. Pellegrino, *Nat. Protoc.* **18**, 783 (2023)
41. A.G. Roca, L. Gutiérrez, H. Gavilán, M.E. Fortes Brollo, S. Veintemillas-Verdaguer, M. del P. Morales, *Adv. Drug Deliv. Rev.* **138**, 68 (2019)
42. A. Varma, A.S. Mukasyan, A.S. Rogachev, K.V. Manukyan, *Chem. Rev.* **116**, 14493 (2016)
43. A. Sutka, G. Mezinskis, *Front. Mater. Sci.* **6**, 128 (2012)
44. K. Deshpande, A. Mukasyan, A. Varma, *Chem. Mater.* **16**, 4896 (2004)
45. C. Cannas, A. Ardu, D. Niznansky, D. Peddis, G. Piccaluga, A. Musinu, *J. Solgel Sci. Technol.* **60**, 266 (2011)
46. K. Deshpande, M. Nersesyan, A. Mukasyan, A. Varma, *Ind. Eng. Chem. Res.* **44**, 6196 (2005)
47. S.J. Kashyap, R. Sankannavar, G.M. Madhu, *Mater. Chem. Phys.* **286**, 126118 (2022)
48. X. Zhang, D. Han, Z. Hua, S. Yang, *J. Alloys Compd.* **684**, 120 (2016)
49. Z.I. Takai, M.K. Mustafa, S. Asman, K.A. Sekak, *Int. J. Nanoelectron. Mater.* **12**, 37 (2019)
50. P. Lv, H. Zhao, Z. Zeng, J. Wang, T. Zhang, X. Li, *J. Power Sources* **259**, 92 (2014)
51. E. Carlos, R. Martins, E. Fortunato, R. Branquinho, *Chem. Eur. J.* **26**, 9099 (2020)
52. M.F. Silva, L.A.S. De Oliveira, M.A. Ciciliati, L.T. Silva, B.S. Pereira, A.A.W. Hechenleitner, D.M.F. Oliveira, K.R. Pirota, F.F. Ivashita, A. Paesano, J. Martin Pastor, J. Iñaki Pérez-Landazábal, E.A.G. Pineda, *J. Appl. Phys.* **114**(10), 104311 (2013)
53. W. Dong, C. Zhu, *J. Mater. Chem.* **12**, 1676 (2002)
54. A. Varma, A.S. Mukasyan, K.T. Deshpande, P. Pranda, P.R. Erri, "Combustion Synthesis of Nanoscale Oxide Powders: Mechanism, Characterization and Properties," in *Mater. Res. Soc. Symp. Proc.* **800**, ed. by R.W. Armstrong, N.N. Thadhani, W.H. Wilson, J.J. Gilman, Z. Munir, R.L. Simpson (Materials Research Society, Warrendale, 2003), pp. 127–138
55. H. Aali, S. Mollazadeh, J.V. Khaki, *Ceram. Int.* **44**, 20267 (2018)
56. M. Radpour, S. Alamolhoda, S.M. Masoudpanah, *Ceram. Int.* **43**, 13729 (2017)
57. R. Ianoş, A. Tăculescu, C. Păcurariu, I. Lazău, *J. Am. Ceram. Soc.* **95**, 2236 (2012)
58. C.F. Holder, R.E. Schaak, *ACS Nano* **13**, 7359 (2019)
59. R. Frison, G. Cernuto, A. Cervellino, O. Zaharko, G.M. Colonna, A. Guagliardi, N. Masciocchi, *Chem. Mater.* **25**, 4820 (2013)
60. G. Muscas, G. Concas, C. Cannas, A. Musinu, A. Ardu, F. Orrù, D. Fiorani, S. Laureti, D. Rinaldi, G. Piccaluga, D. Peddis, *J. Phys. Chem. C* **117**, 23378 (2013)
61. E. Verwey, *Nature* **144**, 327 (1939)
62. C. Cannas, A. Musinu, D. Peddis, G. Piccaluga, *J. Nanopart. Res.* **6**, 223 (2004)
63. S.E. Sandler, B.D. Fellows, O.T. Mefford, *Anal. Chem.* **91**, 14159 (2019)
64. B.D. Cullity, C.D. Graham, *Introduction to Magnetic Materials* (Wiley, Hoboken, 2008)
65. H. Zhang, D. Zeng, Z. Liu, *J. Magn. Magn. Mater.* **322**, 2375 (2010)
66. D. Wyrzykowski, E. Hebanowska, G. Nowak-Wiczk, M. Makowski, L. Chmurzyński, *J. Therm. Anal. Calorim.* **104**, 731 (2011)
67. N. Kalaimani, K. Ramya, G. Vinitha, R. Aarthi, C. Ramachandra Raja, *Optik* (Stuttgart) **192**, 162960 (2019)
68. E. Castagnotto, F. Locardi, S. Slimani, D. Peddis, L. Gaggero, M. Ferretti, *Dye. Pigm.* **185**, 108881 (2021)
69. Q. Li, C.W. Kartikowati, S. Horie, T. Ogi, T. Iwaki, K. Okuyama, *Sci. Rep.* **7**, 9894 (2017)
70. D. Hambardzumyan, H. Gyulasaryan, A. Kuzanyan, A. Sargsyan, V. Avagyan, S. Kubrin, A. Manukyan, A.S. Mukasyan, *J. Solgel Sci. Technol.* **111**, 268 (2024)
71. K.V. Manukyan, Y.S. Chen, S. Rouvimov, P. Li, X. Li, S. Dong, X. Liu, J.K. Furdyna, A. Orlov, G.H. Bernstein, W. Porod, S. Roslyakov, A.S. Mukasyan, *J. Phys. Chem. C* **118**, 16264 (2014)
72. C. Meiorin, D. Muraca, K.R. Pirota, M.I. Aranguren, M.A. Mosiewicki, *Eur. Polym. J.* **53**, 90 (2014)
73. A. Omelyanchik, A.S. Kamzin, A.A. Valiullin, V.G. Semenov, S.N. Vereshchagin, M. Volochaev, A. Dubrovskiy, T. Sviridova, I. Kozenkov, E. Dolan, D. Peddis, A. Sokolov, V. Rodionova, *Colloids Surf. A Physicochem. Eng. Asp.* **647**, 129090 (2022)
74. A. Mauro, N. José, O. Landeros, L. Téllez, J. Ana, M. Paniagua, *MRS Adv.* **2024**, 9 (1810)
75. G. Barrera, P. Tiberto, C. Sciancalepore, M. Messori, F. Bondioli, P. Allia, *J. Mater. Sci.* **54**, 8346 (2019)
76. F.C. Voogt, T. Fujii, P.J.M. Smulders, L. Niesen, M.A. James, T. Hibma, *Phys. Rev. B* **60**, 11193 (1999)
77. D.K. Bora, A. Braun, S. Erat, O. Safonova, T. Graule, E.C. Constable, *Curr. Appl. Phys.* **12**, 817 (2012)
78. G. Muscas, P. Anil Kumar, G. Barucca, G. Concas, G. Varvaro, R. Mathieu, D. Peddis, *Nanoscale* **8**, 2081 (2016)
79. P. Maltoni, G. Barucca, B. Rutkowski, M.C. Spadaro, P.E. Jönsson, G. Varvaro, N. Yaacoub, J.A. De Toro, D. Peddis, R. Mathieu, *Small* 20(10), 2304152 (2024). https://doi.org/10.1002/smll.202304152
80. P. Maltoni, T. Sarkar, G. Varvaro, G. Barucca, S.A. Ivanov, D. Peddis, R. Mathieu, *J. Phys. D Appl. Phys.* **54**, 124004 (2021) □